

Platinum equation of state to greater than two terapascals: Experimental data and analytical models

Kyle R. Cochrane ^{*}, Patricia Kalita, Justin L. Brown, Chad A. McCoy, Jeffry W. Gluth ,
Heath L. Hanshaw, Edward Scoglietti, and Marcus D. Knudson
Sandia National Laboratories, Albuquerque, New Mexico 87125, USA

Sven P. Rudin  and Scott D. Crockett 
Los Alamos National Laboratory, Los Alamos, New Mexico 87545, USA



(Received 6 December 2021; revised 17 May 2022; accepted 26 May 2022; published 17 June 2022)

In order to develop a high impedance standard for shock physics applications, we investigated the equation of state (EOS) and shock compression of bulk platinum using canonical *ab initio* molecular dynamics (AIMD) simulations, coupled with experimental data on Sandia’s Z machine. In simulations, we sampled the thermodynamic state space along isotherms ranging from 300 to 100 000 K for densities of 18 to 40 g/cm³. While this rectilinear grid of EOS points was useful for preliminary experimental design, material going outside of the density/temperature space of the AIMD simulations required a SESAME-style, broad-range EOS, which we developed independently and subsequently compared to the AIMD simulations. In the final step we validated the SESAME EOS with experimental shock data to 2177 GPa on Sandia’s Z machine. The theoretical and AIMD results are in excellent agreement with experiments.

DOI: [10.1103/PhysRevB.105.224109](https://doi.org/10.1103/PhysRevB.105.224109)

I. INTRODUCTION

All scientific disciplines require standards with which to gauge unknown quantities. In high-pressure and shock compression physics several materials play the role of standards, or reference materials, some of the most important being SiO₂ [1–3], Al, Cu [4] (dynamic compression), Au [5,6], Pt [6], and Ag and Cu [7] (static compression). In this context platinum, with its simple phase diagram, is an attractive addition to the family of reference materials. The face-centered cubic lattice of the Pt crystal does not display any experimentally observed phase change between absolute zero and the melting point, at 2045 K [8–10].

Another key requirement for impactors/flyers in any shock experiment is a high-fidelity equation of state (EOS), because the pressure generated in the target material is usually extrapolated from a high-fidelity EOS of the impactor by way of impedance matching [11]. In this work we present a SESAME-style, broad-range EOS of platinum which we compare to *ab initio* molecular dynamics (AIMD) simulations and validate with experimental shock data to 2177 GPa on Sandia’s Z machine. This is one step toward verifying the platinum SESAME EOS as a “standards” model.

II. DENSITY FUNCTIONAL THEORY

We conducted first-principles density functional theory (DFT) calculations of the cold curve (0 K) using the Vienna *ab initio* simulation package (VASP) [12–15]. The

exchange-correlation energy was computed with the parametrization of Perdew, Burke, and Ernzerhof for solids (PBEsol) [16]. We used PBEsol instead of PBE [17,18] based on bulk modulus and reference density work presented by Dewaele *et al.* [19] and Corso [20].

In the Kohn-Sham equations, the nuclei were represented by a projector augmented wave (PAW) method [21]. The PAW pseudopotential contained 16 electrons in the valance and we set the cutoff energy for the cold-curve calculations to 1000 eV. We utilized first-order Methfessel-Paxton smearing [22], with a value of $\sigma = 50$ meV, to control partial occupancies for each wave function. The cutoff criterion was 10^{−6} eV. The *k*-point mesh was Monkhorst-Pack [23] 18 × 18 × 18 for a four-atom fcc unit cell which yielded an energy error of 1.6 meV/atom. A third-order Birch-Murnaghan fit gave $V_0 = 15.05 \text{ \AA}^3$, $B_0 = 287$ GPa, and $B'_0 = 5.31$ while a Vinet fit for the same V_0 gave $B_0 = 288$ GPa and $B'_0 = 5.97$. The DFT cold-curve simulations were compared with a subsequent SESAME model (discussed later) and the Vinet fit to data from Fratanduono *et al.* [10] as well as data and theory from Elkin *et al.* [24], and are shown in Fig. 1. As can be seen, the DFT simulations compare well with the SESAME model, the Vinet fit, and other theories.

To further validate the DFT calculations, again using the PBEsol functional, the elastic constants (Fig. 2) were evaluated with the four-atom conventional unit cell, for which the stresses were calculated in response to applied strains. Here the *k*-point mesh was 32 × 32 × 32 and the energy cutoff was 644 eV. The phonons were calculated by the small-displacement method, specifically displacing an atom by 0.03 Å at the experimental volume and by scaled amounts at other volumes. A 6 × 6 × 6 supercell with 216 atoms was

*kcochra@sandia.gov

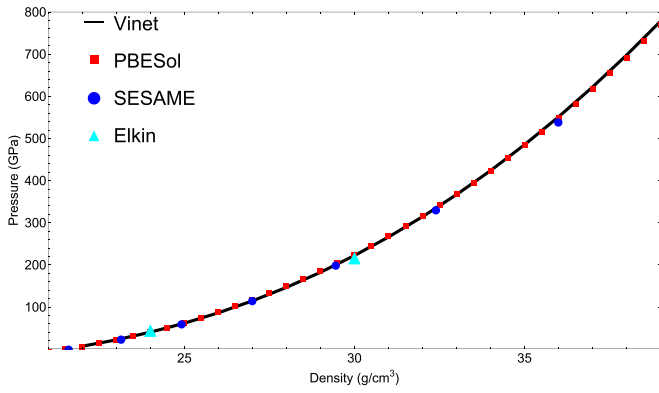


FIG. 1. Platinum cold curve calculated using the PBEsol (red squares) potential. Samples of the independently developed SESAME cold curve are represented by the blue circles. The black line in the main plot is the Vinet fit to data based on [10]. The cyan triangles are selected examples from Fig. 3 of Elkin *et al.* [24]. All calculations are in excellent agreement.

used with an energy cutoff of 294.6 eV and the k -point mesh of $8 \times 8 \times 8$. The phonons were evaluated from the forces using the PHON code [25]. The DFT-calculated elastic constants in Table I compare well with experimental data [26,27]; similarly the DFT-calculated phonon dispersion in Fig. 3 shows good agreement with experimental data [28].

We conducted *ab initio* molecular dynamics simulations (AIMD) simulations in order to create a tabular EOS directly usable in a hydrodynamics code. The AIMD simulations used the 16-electron pseudopotential, PBEsol, and the Mermin generalization of the Kohn-Sham equations to finite temperature [29]. We performed simulations in the canonical (NVT) ensemble along isotherms ranging from 300 to 100 000 K and densities from 18.0 to 40.0 g/cm^3 . In all AIMD, we utilized 108-atom periodic supercells to ensure negligible interaction between the structures simulated and their periodic images. At 50 000 K we reduced the number of atoms to 54, and to 40 at 80 000 K. We carried out property averaging in the Brillouin zone using the Monkhorst-Pack $2 \times 2 \times 2$ in the solid regime and Baldereschi mean-value special k point [30] in the liquid. We used a time step for ion motion of 1.0 fs in the simulations, with velocities scaled to the temperature at each simulation step. The cutoff energy was set to 600 eV, producing an error

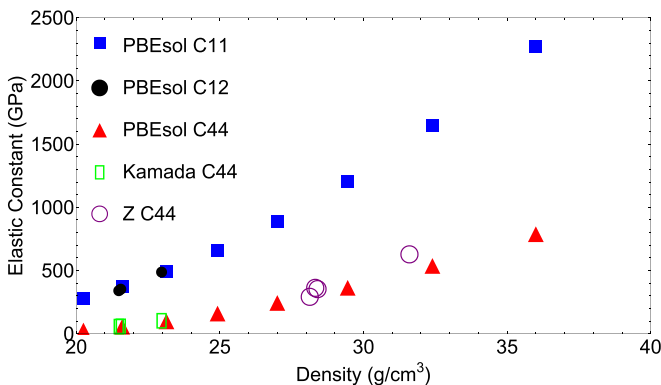


FIG. 2. Elastic constants as a function of density. The size of the open circles is roughly representative of the error bars of the Z data.

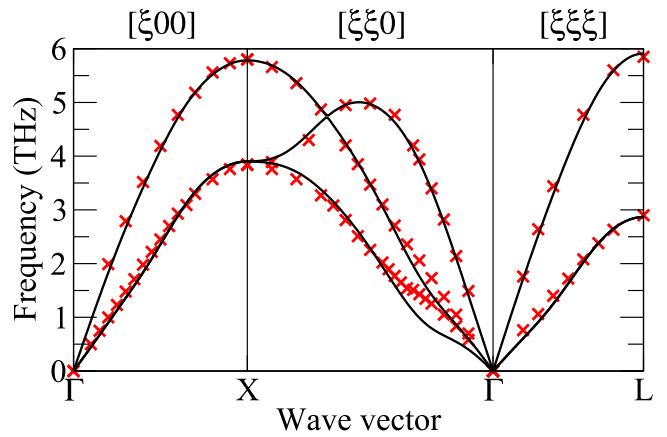


FIG. 3. Phonon dispersion curves of Pt measured at 90 K (red crosses) [28] and calculated in the harmonic approximation (solid black line).

of 0.2 meV. Selected results of this grid of EOS points are shown in Fig. 4.

III. EQUATION OF STATE DESIGN

We attempted to use the DFT-generated table (Supplemental Material [32]) as an EOS model in a hydrodynamics code. While this was adequate for some simulations, the relatively high minimum density (18 g/cm^3) using this grid as a tabular EOS suffered from shortcomings. For example, material releasing from the shocked state reached densities below this minimum and caused the interpolation methods to return spurious results when extrapolating off the grid. Therefore, we developed a new EOS table in the SESAME format [33], SESAME 3732, to give a broader range of densities and temperatures than was feasible to produce with DFT and which

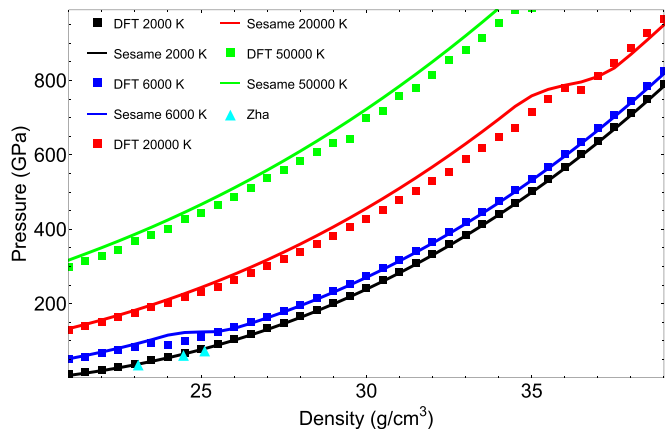


FIG. 4. The different colors represent different isotherms. The solid lines were taken from the SESAME table and the squares were taken from the DFT-generated grid. The squares also show the density grid resolution for the DFT-generated table. The location of the DFT-approximated melt line is seen at the discontinuity along the 6000 K and 20 000 K isotherms. For a comparison, several points from experiments by Zha *et al.* [31] at 1900 K are shown as cyan triangles. The theory and simulations are very close to the experimental data.

TABLE I. Calculated elastic constants at zero temperature. Comparison to inelastic x-ray scattering data [26] and Z machine isentropic compression data [27].

ρ (g/cm ³)	V (Å ³)	P (GPa)	C_{11} (GPa)	C_{12} (GPa)	C_{44} (GPa)
DFT					
20.25	16.00	-15	269	190	42
21.60	15.00	1	364	254	72
23.14	14.00	25	488	340	115
24.92	13.00	62	655	456	176
27.00	12.00	118	882	618	260
29.45	11.00	205	1201	846	380
32.40	10.00	339	1640	1178	553
36.00	9.00	553	2268	1673	804
40.50	8.00	904	3183	2445	1175
46.29	7.00	1504	4556	3699	1724
IXS					
21.48	15.09	0	349	246	73
21.55	15.04	1	361	261	75
22.97	14.11	21	496	372	119
Z machine					
28.13	11.52	159.4			304
28.32	11.44	161.8			375
28.40	11.41	164.2			365
28.80	10.25	312.0			640

was required for many types of simulations. As a test of the EOS building tools, we developed the SESAME EOS table independently of the DFT work and compared the table with DFT after completion.

In the development of the SESAME EOS, we used a standard three-term decomposition of the Helmholtz free energy: cold curve, ion thermal, and electron thermal components, i.e., $F(T, V) = F_{cold}(V) + F_{ion}(T, V) + F_{electron}(T, V)$ [33]. The ion thermal component used a Debye approximation for the solid [34] and a corrected Debye [35] approximation for the fluid [36]. The thermodynamic Grüneisen gamma and reference Debye temperature in the ion thermal model were set by matching isobaric expansion data [37] and specific heat [38]. The cold curve was determined via a Mie Grüneisen approximation by matching a simple quadratic to the experimental U_s/U_p shock data. The intercept of the quadratic was fixed to match the adiabatic bulk modulus from ultrasonic data [37]. The derivative of the Grüneisen gamma (Γ) parameter with respect to density was obtained by matching to the room temperature diamond anvil cell data [19]. The electron thermal component was determined using the Thomas-Fermi-Dirac (TFD) model.

IV. AIMD-SESAME COMPARISON

When we compared select isotherms (0 K, 2000, 6000, 20 000, and 50 000 K) between SESAME 3732 and DFT we found that there was a systematic offset in pressure and energy in the fluid region for 2000 K and above.

$$\Gamma = V \left(\frac{dP}{dT} \right) \bigg|_V. \quad (1)$$

We also compared the Grüneisen Γ as defined in Eq. (1) where P is pressure, T is temperature, E is specific internal energy, and V is specific volume. Results are shown in Fig. 5.

When comparing the selected isotherms, dP/dT obtained from DFT and SESAME were found to be quite similar at temperatures between 2000 and 20 000 K. However, dE/dT from DFT was found to be larger than, similar to, and slightly lower than that from SESAME at 2000, 6000, and 20 000 K, respectively. The 6000 K isotherm's dP/dT and dE/dT are approximately equal. The 20 000 K DFT isotherm's dE/dT

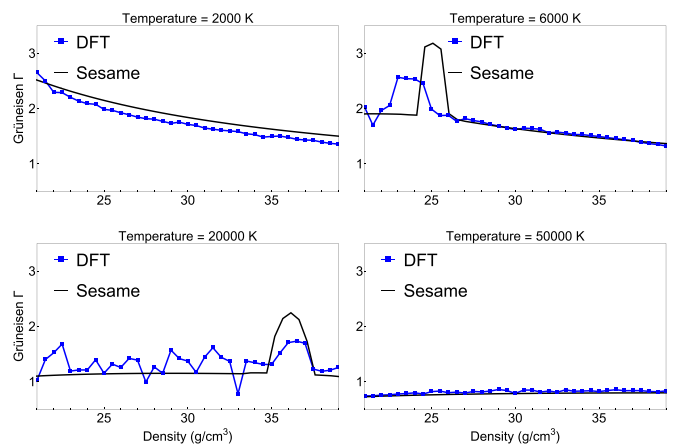


FIG. 5. Grüneisen Γ as a function of density for several isotherms. The Γ calculated from the DFT-generated table compares well with the SESAME table in the liquid. The large spike at 25 g/cm³ along the 6000 K isotherm and at 36 g/cm³ along the 20 000 K isotherm is the melt transition.

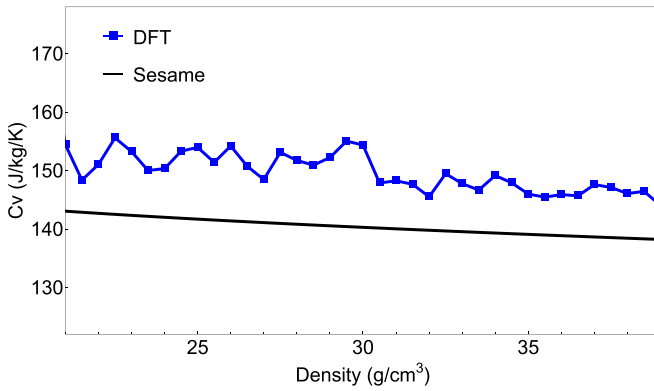


FIG. 6. Specific heat as a function of density along the 2000 K isotherm. The specific heat is about 10% higher in DFT than in SESAME and is reflected in the Grüneisen Γ at this temperature. The oscillations in the DFT specific heat are from taking a finite-difference derivative of stochastic simulations.

is just slightly lower than SESAME while dP/dT is about the same. For the 50 000 K isotherm both dP/dT and dE/dT from DFT were found to be lower than that from SESAME, resulting in a cancellation of differences such that the inferred Gamma from both appeared to be similar.

These differences may be explained by either (i) a difference in the value of Gamma used in the liquid ion model, compensated by the cold-curve pressure, or (ii) an underestimation of the specific heat in the TFD thermal electronic model.

In Fig. 4, each line is an isotherm between 2000 K and 50 000 K with a DFT density point every 0.5 g/cm^3 . The discontinuity in the 6000 K and 20 000 K isotherms is the melt transition as approximated by DFT given the cell size of our simulations, or the Lindemann melt approximation used in SESAME. In the AIMD simulations, the structure started as solid and, if it melted, all temperatures above that for a given density were then started as liquid (usually from the output of the previous simulation). As such, the DFT melt transition should be considered an upper bound in temperature. Nonetheless the SESAME EOS melt density is consistent with DFT. The SESAME pressures for a given density and temperature compare well with the DFT simulations in the solid in contrast to the liquid, where the SESAME pressures are systematically higher, as seen in Fig. 4. This leads us to the conclusion that the SESAME tables use an isothermal bulk modulus in the liquid that is different from that calculated by DFT.

Based on the difference in the Grüneisen Γ from Fig. 5, we compared the specific heat, C_v , of SESAME vs DFT along the 2000 K isotherm. The results are shown in Fig. 6. The DFT C_v is calculated by finite difference between two isotherms. The SESAME specific heat is fitted to experimental calorimetric data for the solid leveraging a Debye model for the ion thermal response and a TFD model for the electron thermal contributions. At $T/T_{melt} = 1$, the ion thermal incorporates a fixed entropy change of melt ($\Delta S = 0.8$) and then smoothly transitions to an ideal gas. As can be seen, the values are different and contribute to the difference in temperature along

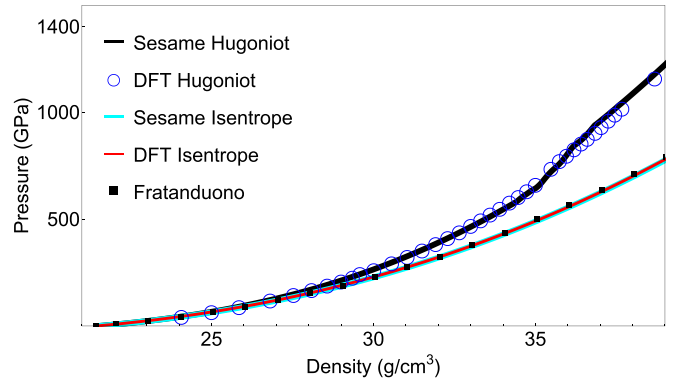


FIG. 7. Hugoniot and isentrope calculated from DFT and SESAME EOSs. The isentrope is virtually identical in pressure/density space. The DFT-calculated isentrope values compare well with experimental data [10].

the isentrope which is discussed later.

$$E - E_0 = (P + P_0)(V_0 - V)/2. \quad (2)$$

The Rankine-Hugoniot energy jump condition can be written as Eq. (2) where E , P , and V are the specific energy, pressure, and specific volume of the material and E_0 , P_0 , and V_0 are the reference state. We used this jump condition to calculate the Hugoniot for both the DFT and SESAME EOS; results are shown in Fig. 7. Both Hugoniots compare quite well with each other in $P(\rho)$ space. The principal isentrope, which remains entirely in the solid, exhibits minimal differences in pressure/density space. However, differences due to specific heat become apparent when viewed in pressure/temperature space (Fig. 8). Given the nature of DFT as apposed to a SESAME-style analytical model, we would expect the DFT to be more accurate but need to confirm this with experimental data.

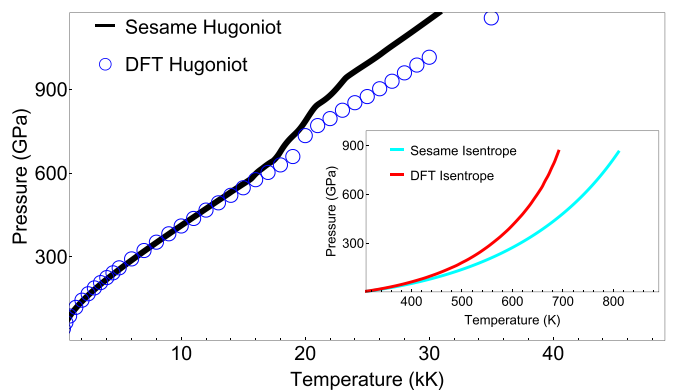


FIG. 8. Hugoniot and isentrope calculated from DFT and SESAME EOSs in pressure/temperature space. The Hugoniot compares well in pressure/temperature space until melt. The difference in the specific heat of liquid causes the two Hugoniots to diverge above the melt boundary. In the inset, the isentropes calculated from the DFT and SESAME EOSs show a clear difference in the specific heat.

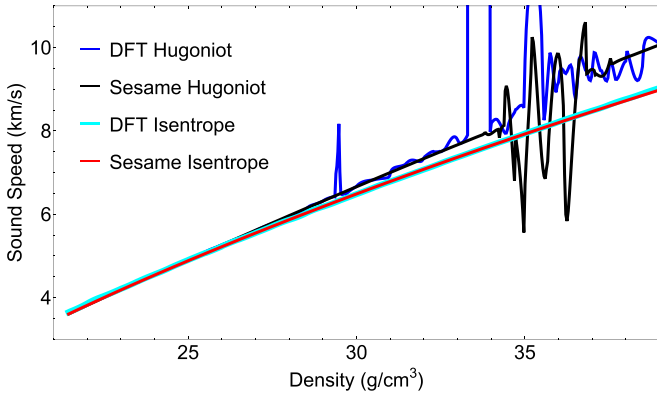


FIG. 9. Sound speeds calculated from the DFT and SESAME EOSs. The large oscillations in the sound speeds are from the melt transition. The sound speeds of both models along the isentrope lie within the thickness of the lines used in the figure.

Finally, using Eq. (3),

$$C_s^2 = \left. \frac{dP}{d\rho} \right|_s = \left. \frac{dP}{d\rho} \right|_T + \frac{\left(\left. \frac{dP}{dT} \right|_\rho \right)^2}{\rho^2 \left. \frac{dE}{dT} \right|_\rho} T, \quad (3)$$

we calculated the sound speed along the Hugoniot and isentrope for both EOSs (Fig. 9). The sound speeds are comparable for both models despite having a difference in specific heat. This may be attributed to the fact that the isentrope is a path-dependent quantity while the sound speed is not, and thus, the integrated effect is evident in the $P(T)$ figure. The large oscillations at 35 g/cm^3 are due to the melt transition. Near 40 g/cm^3 , the sound speed calculated from the DFT-generated table continues to have large oscillations and is because of the finite-difference style of derivative used on the more sparsely populated DFT EOS and the statistical uncertainty in the pressure and energy of the DFT EOS.

V. EXPERIMENTS: Z MACHINE

To validate the EOS table, we carried out shock compression experiments using the Sandia Z Machine [39]. The Z machine is a pulsed power system capable of producing shaped current pulses and induced magnetic fields of more than 20 MA and 10 MG, respectively. We can utilize the Z machine to accelerate aluminum flyer plates up to 40 km/s [40] to probe the Hugoniot states. In this study, the highest velocity was 30.79 km/s.

In the present experiments, we generated shocked states of up to 2177 GPa using geometries illustrated in Fig. 10: the coaxial geometry and the 2-sided stripline geometry for extremely high velocity shots. The Al flyer plate is shocklessly accelerated toward the target stack, composed of a sample of platinum (Pt, $\sim 300\text{--}400 \mu\text{m}$, $\rho_0 21.45 \text{ g/cm}^3$) and either a polymethylpentene (also known by its trade name TPX) or α -quartz window. While the backside of the flyer was melted by the high driving current, the impact side of the flyer remained at solid density [40], producing a steady shock in the sample.

We used two push-pull velocity interferometer systems for any reflector (VISAR) [41,42] with dual velocity per fringe

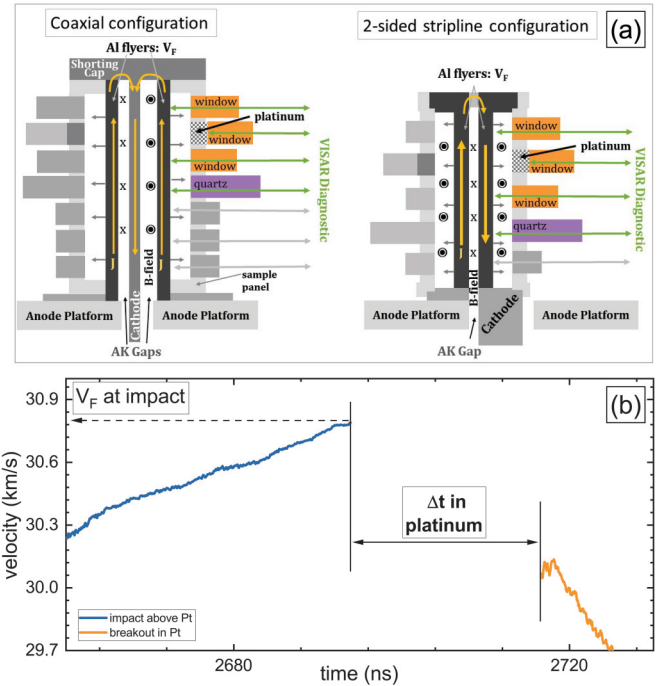


FIG. 10. Shock experiments on the Z machine. (a) The two experimental configurations used in this work to generate lower pressure data (coaxial configuration) and higher pressure data (stripline configuration). (b) Processed VISAR signals showing impact on a transparent window above and below the Pt sample and shock breakout on the Pt sample itself.

(VPF) capabilities to measure velocity up to impact at the target (Fig. 10). Three VISAR signals are typically recorded for the sample eliminating 2π ambiguities and providing redundant measurements for improved precision. We typically use three different VPFs on the sample: 0.5878 km/s/f, 1.0632 km/s/f, and 1.4317 km/s/f.

Since the sample is opaque to VISAR light, impact time was determined for both the opaque and transparent samples from fiducials observed in transparent windows adjacent to the opaque sample stack. Impact time was then corrected for any measured tilt of the impact plane and for the relative offset of the 2 windows and the sample (typically a few μm). Shock breakout was directly monitored at the back surface of the opaque sample, through a window. We then calculated the sample shock velocity (U_s) using the transit time determined from the VISAR fiducials and the measured thickness. The shock wave was also monitored in a thick quartz witness window, which allowed us to determine any correction due to acceleration of the flyer and apply this correction to the U_s of the sample.

For the transit time measurements, the uncertainty was less than 0.5%. In the VISAR analysis, we used a transit time determination of the shock velocity using unprocessed VISAR signals. To calculate transit time, we determined when the raw VISAR signal had a change larger than the standard deviation of the signal prior to the change. That marked our impact and our transit into the backing TPX or α -quartz window. We used the standard deviation from the transit time determination,

TABLE II. Linear fit parameters and the off-diagonal term in the covariance matrix for the fit parameters of the Al flyer. $U_S = C_0 + s_1 U_P$.

Flyer	C_0 (km/s)	s_1	$\sigma C_0 \sigma s_1 \times 10^3$
Al	6.322 ± 0.231	1.188 ± 0.020	-4.605

along with the uncertainty in the sample thickness, to determine the uncertainty in the shock velocity.

In a simple shock event the conservation of mass, momentum, and energy is described by Rankine-Hugoniot jump conditions [Eqs. (2), (4), and (5)], where P , ρ , and E are the pressure, density, and specific internal energy, respectively, of the shocked material relative to its initial state, denoted with the subscript 0. P , ρ , and E are related by the shock velocity (U_S) and particle velocity (U_P) of the shock wave. By definition, the principal Hugoniot initiates from ambient conditions.

$$\frac{\rho}{\rho_0} = \frac{U_S}{U_S - U_P}, \quad (4)$$

$$P = \rho_0 U_S U_P. \quad (5)$$

Knowing the initial densities of the sample and the Al flyer plate and measuring the flyer V_F and the sample U_S , we calculated the sample Hugoniot state density, pressure, and particle velocity (U_P). The Hugoniot state was determined using a Monte Carlo impedance matching analysis [43,44] to solve the Rankine-Hugoniot equations. The Monte Carlo impedance matching (MCIM) method accounted for the correlated and uncorrelated uncertainties in the experimental measurement and the Al Hugoniot standard. In the MCIM, uncorrelated random numbers with one standard deviation equal to the measurement uncertainty were used to adjust the flyer velocity, the shock velocity, and the initial densities about their mean value. Correlated random numbers adjust the fit parameters to the aluminum Hugoniot standard. The linear fit parameters and correlation between the parameters for the aluminum standard are listed in Table II.

The impedance matching calculation was performed to determine U_P , ρ , and P in the Hugoniot state. The data were saved and the calculation restarted using new random numbers. A database of Hugoniot states was built for 10^7 iterations and the final Hugoniot state was calculated as the mean with 1 standard deviation of the distribution as the uncertainty. The principal Hugoniot data for platinum samples

experimentally measured on the Z machine are listed in Table III.

Platinum release states were determined from the measured shock velocity in the quartz backing the samples. As quartz has been highly constrained for shock pressures in the range 200–1600 GPa [1], we were able to use the known quartz Hugoniot to determine the pressure and particle velocity in the quartz window. To determine the state of platinum at the end point of the release curve, the average velocity determined from the platinum shock transit time was corrected for acceleration over the entire duration of the transit. This acceleration correction was carried out by relating the measured instantaneous shock velocity in an adjacent window to the average shock velocity in the platinum using a zeroth-order correction $U_{S,P}^{inst}(t) = \frac{\langle U_{S,P} \rangle}{\langle U_{S,W} \rangle} U_{S,W}^{inst}(t)$ where $U_{S,P}^{inst}$ is the calculated instantaneous shock velocity in the platinum, and $\langle U_{S,P} \rangle$ and $\langle U_{S,W} \rangle$ are the average shock velocity in the window [45]. The instantaneous shock velocity at breakout from the platinum was taken as the final value of the platinum data after fitting over 0.5 ns to mitigate random noise in the data.

The shock velocity in the quartz used for the impedance matching calculation was determined by fitting the measured quartz shock velocity over the first 1.0 ns of data after the shock in the anvil reached a steady state. This was then propagated backward through the glue to determine the velocity which would have been measured if the samples were in intimate contact with no glue layer [46]. In this experiment, the glue layer was measured to be $\sim 1 \mu\text{m}$ and the corresponding correction to the quartz shock velocity was 0.012 km/s (compared to the measurement uncertainty of 0.026 km/s). Pressure and particle velocity uncertainties in the release state were determined using a Monte Carlo routine to account for covariance of the quartz Hugoniot fit and the measurement uncertainty.

Next, we compare the DFT and SESAME models with experimental data; the results are shown in Fig. 11. The SESAME EOS is within the error bars of the experimental values along the Hugoniot with the exception of the point at $\approx 41 \text{ g/cm}^3$. It is unclear why this point does not follow the expected $P(\rho)$ curve and warrants further examination such as a second experiment. The values interpolated from the DFT grid, as well as the points directly calculated via the jump condition, overlie the SESAME results well and both are within the experimental uncertainty. Because the DFT grid stopped at 40 g/cm^3 , additional calculations were specifically done to test DFT at the highest pressure. Again, DFT pressure matched SESAME.

TABLE III. Experimental Hugoniot results. V_f is the aluminum flyer velocity. U_P and U_S are the platinum particle and shock velocities. ρ and P are the platinum shock density and pressure.

V_f (km/s)	U_P (km/s)	U_S (km/s)	ρ (g/cm ³)	P (GPa)
21.58 ± 0.03	4.93 ± 0.04	11.12 ± 0.08	38.54 ± 0.42	1175 ± 7
23.04 ± 0.03	5.29 ± 0.04	11.58 ± 0.06	39.50 ± 0.35	1315 ± 8
23.67 ± 0.07	5.49 ± 0.05	11.64 ± 0.12	40.60 ± 0.67	1371 ± 9
25.05 ± 0.08	5.82 ± 0.05	12.11 ± 0.08	41.33 ± 0.50	1513 ± 10
30.79 ± 0.03	7.29 ± 0.07	13.93 ± 0.11	44.99 ± 0.71	2177 ± 15
30.79 ± 0.02	7.27 ± 0.07	13.88 ± 0.11	45.09 ± 0.70	2165 ± 15

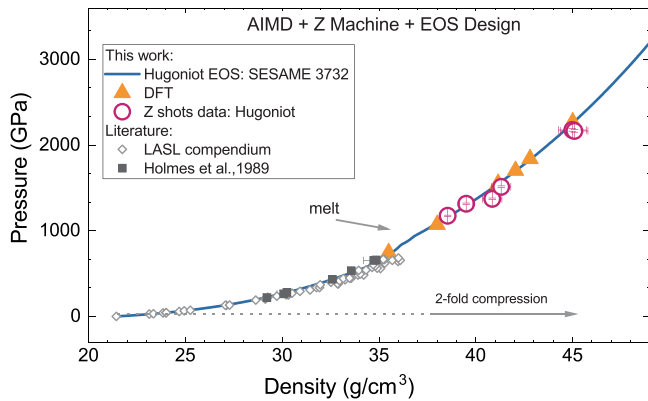


FIG. 11. Comparison of the experimental Hugoniot data by Holmes *et al.* [9] and the Z data with the calculated EOS and DFT points. With the exception of the one data point near 41 g/cm³, the SESAME Hugoniot is within the error bars of the experimental data.

In two of the Z experiments, we obtained release data into the quartz which allowed us to further evaluate the SESAME model and the DFT simulations. The top rows of Table IV list the measured shock velocity at breakout in the platinum, the subsequent shock velocity in the quartz upon release, and the inferred particle velocity and pressure in the quartz based on the quartz standard [3]. Note that the error bars associated with the platinum shock velocities shown in Table IV are larger than those in Table I. The uncertainty in the inferred shock velocity at breakout is greater than at the impact surface because a rarefaction wave had overtaken the shock front in the platinum prior to breakout into the quartz window; uncertainty in the timing of the rarefaction overtake results in larger uncertainty the shock velocity at breakout. To evaluate the SESAME model we calculated release isentropes starting at shock pressures along the SESAME Hugoniot that corresponded to the measured shock velocity in the platinum. The intersection of these release curves with the quartz standard resulted in the predicted quartz shock velocities, particle velocities, and pressures listed in the middle rows of Table IV. In both cases the measured shocked state in the quartz is slightly higher than the SESAME model prediction. A similar process was followed to evaluate the DFT simulations using targeted simulations and the quasi-isentropic expansion approxima-

tion of the Rankine-Hugoniot jump condition. The results for the predicted quartz shock velocities, particle velocities, and pressures are listed in the bottom rows of Table IV. The DFT results are in much better agreement with experiment, and in contrast to the SESAME model, the measured shock state in the quartz is slightly lower than the DFT simulations. The better agreement between the release experiments and DFT suggests that DFT provides a better description of the off-Hugoniot behavior in the liquid.

VI. CONCLUSION

We used density functional theory AIMD methods and SESAME analytical tools to build two different platinum equations of state. The Hugoniot, isentrope, and sound speed values compare quite well between the two despite having the different $P(T)$ values as shown in Fig. 4 or the different specific heat values as shown in Fig. 6, etc., which suggests a canceling error. Both models compared quite well with our experimental data to over 2.1 TPa as shown in Fig. 11. Additionally, the good agreement between DFT-calculated elastic constants and experiment lends further confidence to the analytical models. The wide-ranging SESAME EOS allows access to lower density and higher temperature regimes than the DFT table, thereby allowing simulation of a wider variety of experiments, particularly in regimes where DFT calculations are computationally intractable. Because the SESAME models are based on a Debye model we would expect the DFT C_v to be more accurate. However, we need to measure the temperature along the isentrope in order to confirm this. Finally, in this work we establish platinum as a standard for shock experiments. However, comparisons with a more diverse set of experimental data are needed before the model can be considered a standard in other regimes (i.e., off-Hugoniot).

ACKNOWLEDGMENTS

We thank John Carpenter (SNL) for extensive discussions on building a standards model. Work was performed in part using the Sierra computer at Lawrence Livermore National Laboratory. Sierra is operated for the U.S. Department of Energy’s National Nuclear Security Administration. Lawrence Livermore National Laboratory operates under the

TABLE IV. Quartz release.

U_S^{Pt} (km/s)	U_S^Q (km/s)	U_P^Q (km/s)	p^Q (GPa)
Experiment			
11.62 ± 0.16	15.84 ± 0.026	8.73 ± 0.019	366 ± 1.4
11.93 ± 0.21	16.41 ± 0.026	9.14 ± 0.018	397 ± 1.4
SESAME 3732			
11.62 ± 0.16	15.55 ± 0.23	8.53 ± 0.16	351.3 ± 11.8
11.93 ± 0.21	15.98 ± 0.29	8.84 ± 0.21	374.3 ± 15.6
DFT			
11.62 ± 0.16	15.92 ± 0.23	8.79 ± 0.16	370.8 ± 11.8
11.93 ± 0.21	16.58 ± 0.29	9.27 ± 0.21	407.2 ± 15.6

auspices of the U.S. Department of Energy under Contract No. DE-AC52-07NA27344. Work at Los Alamos National Laboratory was supported by the U.S. Department of Energy's National Nuclear Security Administration through Contract No. 89233218CNA000001. Sandia National Laboratories is a multimission laboratory managed and operated by National Technology and Engineering Solutions of Sandia, LLC, a

wholly owned subsidiary of Honeywell International, Inc., for the U.S. Department of Energy's National Nuclear Security Administration under Contract No. DE-NA0003525. This paper describes objective technical results and analysis. Any subjective views or opinions that might be expressed in the paper do not necessarily represent the views of the U.S. Department of Energy or the United States Government.

-
- [1] M. D. Knudson and M. P. Desjarlais, Shock Compression of Quartz to 1.6 TPa: Redefining a Pressure Standard, *Phys. Rev. Lett.* **103**, 225501 (2009).
- [2] M. D. Knudson and M. P. Desjarlais, Adiabatic release measurements in α -quartz between 300 and 1200 GPa: Characterization of α -quartz as a shock standard in the multimegabar regime, *Phys. Rev. B* **88**, 184107 (2013).
- [3] M. P. Desjarlais, M. D. Knudson, and K. R. Cochrane, Extension of the Hugoniot and analytical release model of α -quartz to 0.2–3 TPa, *J. Appl. Phys.* **122**, 035903 (2017).
- [4] R. G. Kraus, J.-P. Davis, C. T. Seagle, D. E. Fratanduono, D. C. Swift, J. L. Brown, and J. H. Eggert, Dynamic compression of copper to over 450 GPa: A high-pressure standard, *Phys. Rev. B* **93**, 134105 (2016).
- [5] O. L. Anderson, D. G. Isaak, and S. Yamamoto, Anharmonicity and the equation of state for gold, *J. Appl. Phys.* **65**, 1534 (1989).
- [6] Y. W. Fei, A. Ricolleau, M. Frank, K. Mibe, G. Y. Shen, and V. Prakapenka, Toward an internally consistent pressure scale, *Proc. Natl. Acad. Sci. U.S.A.* **104**, 9182 (2007).
- [7] W. J. Carter, S. P. Marsh, J. N. Fritz, and R. G. McQueen, Accurate characterization of the high-pressure environment, in *National Bureau of Standards Special Publication*, edited by E. C. Lloyd, Vol. 326 (National Bureau of Standards, Washington D.C., 1971), pp. 147–158.
- [8] S. Anzellini, V. Monteseuro, E. Bandiello, A. Dewaele, L. Burakovsky, and D. Errandonea, *In situ* characterization of the high pressure–high temperature melting curve of platinum, *Sci. Rep.* **9**, 13034 (2019).
- [9] N. C. Holmes, J. A. Moriarty, G. R. Gathers, and W. J. Nellis, The equation of state of platinum to 660 GPa (6.6 Mbar), *J. Appl. Phys.* **66**, 2962 (1989).
- [10] D. E. Fratanduono, M. Millot, D. G. Braun, S. J. Ali, A. Fernandez-Pañella, C. T. Seagle, J.-P. Davis, J. L. Brown, Y. Akahama, R. G. Kraus, M. C. Marshall, R. F. Smith, E. F. O'Bannon, J. M. McNaney, and J. H. Eggert, Establishing gold and platinum standards to 1 terapascal using shockless compression, *Science* **372**, 1063 (2021).
- [11] Y. B. Zel'dovich and Y. P. Raizer, *Physics of Shock Waves and High-Temperature Hydrodynamic Phenomena* (Dover, Mineola, NY, 2002).
- [12] G. Kresse and J. Hafner, *Ab initio* molecular dynamics for liquid metals, *Phys. Rev. B* **47**, 558 (1993).
- [13] G. Kresse and J. Hafner, *Ab initio* molecular-dynamics simulation of the liquid-metal–amorphous-semiconductor transition in germanium, *Phys. Rev. B* **49**, 14251 (1994).
- [14] G. Kresse and J. Furthmüller, Efficient iterative schemes for *ab initio* total-energy calculations using a plane-wave basis set, *Phys. Rev. B* **54**, 11169 (1996).
- [15] G. Kresse and J. Furthmüller, Efficiency of *ab initio* total energy calculations for metals and semiconductors using a plane-wave basis set, *Comput. Mater. Sci.* **6**, 15 (1996).
- [16] J. P. Perdew, A. Ruzsinszky, G. I. Csonka, O. A. Vydrov, G. E. Scuseria, L. A. Constantin, X. Zhou, and K. Burke, Restoring the Density-Gradient Expansion for Exchange in Solids and Surfaces, *Phys. Rev. Lett.* **100**, 136406 (2008).
- [17] J. P. Perdew, K. Burke, and M. Ernzerhof, Generalized Gradient Approximation Made Simple, *Phys. Rev. Lett.* **77**, 3865 (1996).
- [18] J. P. Perdew, K. Burke, and M. Ernzerhof, Generalized Gradient Approximation Made Simple [Phys. Rev. Lett. 77, 3865 (1996)], *Phys. Rev. Lett.* **78**, 1396(E) (1997).
- [19] A. Dewaele, M. Torrent, P. Loubeyre, and M. Mezouar, Compression curves of transition metals in the Mbar range: Experiments and projector augmented-wave calculations, *Phys. Rev. B* **78**, 104102 (2008).
- [20] A. D. Corso, *Ab initio* phonon dispersions of transition and noble metals: Effects of the exchange and correlation functional, *J. Phys.: Condens. Matter* **25**, 145401 (2013).
- [21] P. E. Blöchl, Projector augmented-wave method, *Phys. Rev. B* **50**, 17953 (1994).
- [22] M. Methfessel and A. T. Paxton, High-precision sampling for Brillouin-zone integration in metals, *Phys. Rev. B* **40**, 3616 (1989).
- [23] H. J. Monkhorst and J. D. Pack, Special points for Brillouin-zone integrations, *Phys. Rev. B* **13**, 5188 (1976).
- [24] V. M. Elkin, V. N. Mikhaylov, A. A. Ovechkin, and N. A. Smirnov, A wide-range multiphase equation of state for platinum, *J. Phys.: Condens. Matter* **32**, 435403 (2020).
- [25] D. Alfè, PHON: A program to calculate phonons using the small displacement method, *Comput. Phys. Commun.* **180**, 2622 (2009).
- [26] S. Kamada, H. Fukui, A. Yoneda, H. Gomi, F. Maeda, S. Tsutsui, H. Uchiyama, N. Hirao, D. Ishikawa, and A. Q. Baron, Elastic constants of single-crystal Pt measured up to 20 GPa based on inelastic x-ray scattering: Implication for the establishment of an equation of state, *C. R. Geosci.* **351**, 236 (2019).
- [27] J. L. Brown, J. P. Davis, and C. T. Seagle, Multi-megabar dynamic strength measurements of Ta, Au, Pt, and Ir, *J. Dyn. Behav. Mater.* **7**, 196 (2021).
- [28] D. H. Dutton, B. N. Brockhouse, and A. P. Miller, Crystal dynamics of platinum by inelastic neutron scattering, *Can. J. Phys.* **50**, 2915 (1972).
- [29] N. D. Mermin, Thermal properties of the inhomogeneous electron gas, *Phys. Rev.* **137**, A1441 (1965).
- [30] A. Baldereschi, Mean-value point in the Brillouin zone, *Phys. Rev. B* **7**, 5212 (1973).

- [31] C.-S. Zha, M. Kenji, W. A. Bassett, O. Tschauner, H.-K. Mao, and R. J. Hemley, *P-V-T* equation of state of platinum to 80 GPa and 1900 K from internal resistive heating/x-ray diffraction measurements, *J. Appl. Phys.* **103**, 054908 (2008).
- [32] See Supplemental Material at <http://link.aps.org/supplemental/10.1103/PhysRevB.105.224109> for the DFT-generated EOS.
- [33] S. P. Lyon and J. D. Johnson, *T-1 Handbook, the SESAME Equation of State Library*, Vols. 1 and 2, LA-UR-92-3407 (Los Alamos National Laboratory, Los Alamos, NM, 1998).
- [34] C. Kittel, editor, *Introduction to Solid State Physics*, 8th ed. (Wiley Press, New York, NY, 2005), p. 704.
- [35] P. Debye, Zur theorie der spezifischen wärmen, *Ann. Phys.* **344**, 789 (1912).
- [36] J. D. Johnson, A generic model for the ionic contribution to the equation of state, *High Press. Res.* **6**, 277 (1991).
- [37] G. Simmons and H. Wang, editors, *Single-Crystal Elastic Constants and Aggregate Properties: A Handbook* (MIT Press, Cambridge, MA, 1971), p. 370.
- [38] F. Simon and W. Zeidler, Investigation on the specific heat at low temperatures: The specific heat of sodium, potassium, molybdenum and platinum, *Z. Physika. Chem.* **123U**, 383 (1926).
- [39] D. B. Sinars, M. A. Sweeney, C. S. Alexander, D. J. Ampleford, T. Ao, J. P. Apruzese, C. Aragon, D. J. Armstrong, K. N. Austin, T. J. Awe, A. D. Baczewski, J. E. Bailey, K. L. Baker, C. R. Ball, H. T. Barclay, S. Beatty, K. Beckwith, K. S. Bell, J. F. Benage Jr., N. L. Bennett *et al.*, Review of pulsed power-driven high energy density physics research on Z at Sandia, *Phys. Plasmas* **27**, 070501 (2020).
- [40] R. W. Lemke, M. D. Knudson, D. E. Bliss, K. Cochrane, J.-P. Davis, A. A. Giunta, H. C. Harjes, and S. A. Slutz, Magnetically accelerated, ultrahigh velocity flyer plates for shock wave experiments, *J. Appl. Phys.* **98**, 073530 (2005).
- [41] L. M. Barker and R. E. Hollenbach, Laser interferometer for measuring high velocities of any reflecting surface, *J. Appl. Phys.* **43**, 4669 (1972).
- [42] L. M. Barker and K. W. Schuler, Correction to the velocity-perfringe relationship for the VISAR interferometer, *J. Appl. Phys.* **45**, 3692 (1974).
- [43] S. Root, K. R. Cochrane, J. H. Carpenter, and T. R. Mattsson, Carbon dioxide shock and reshock equation of state data to 8 Mbar: Experiments and simulations, *Phys. Rev. B* **87**, 224102 (2013).
- [44] S. Root, L. Shulenburg, R. W. Lemke, D. H. Dolan, T. R. Mattsson, and M. P. Desjarlais, Shock Response and Phase Transitions of MgO at Planetary Impact Conditions, *Phys. Rev. Lett.* **115**, 198501 (2015).
- [45] D. E. Fratanduono, D. H. Munro, P. M. Celliers, and G. W. Collins, Hugoniot experiments with unsteady waves, *J. Appl. Phys.* **116**, 033517 (2014).
- [46] A. Lazicki, R. A. London, F. Coppari, D. Erskine, H. D. Whitley, K. J. Caspersen, D. E. Fratanduono, M. A. Morales, P. M. Celliers, J. H. Eggert, M. Millot, D. C. Swift, G. W. Collins, S. O. Kucheyev, J. I. Castor, and J. Nilsen, Shock equation of state of ${}^6\text{LiH}$ to 1.1 TPa, *Phys. Rev. B* **96**, 134101 (2017).